Sphingolipids control dermal fibroblast heterogeneity

RESEARCH ARTICLE SUMMARY

LIPIDOMICS

Sphingolipids control dermal fibroblast heterogeneity

Laura Capolupo, Irina Khven, Alex R. Lederer, Luigi Mazzeo, Galina Glousker, Sylvia Ho, Francesco Russo, Jonathan Paz Montoya, Dhaka R. Bhandari, Andrew P. Bowman, Shane R. Ellis, Romain Guiet, Olivier Burri, Johanna Detzner, Johannes Muthing, Krisztian Homicsko, François Kuonen, Michel Gilliet, Bernhard Spengler, Ron M. A. Heeren, G. Paolo Dotto, Gioele La Manno*, Giovanni D'Angelo*

INTRODUCTION: External signals (e.g., hormones, cytokines, and growth factors) and cell-autonomous properties (e.g., the transcriptional and metabolic states of individual cells) concur to determine cell-fate decisions. Although the mode of action of external signals has been detailed extensively in decades of intense research, the molecular bases of cell-autonomous contribution to cell-fate decisions have been traditionally more elusive. Lipids are fundamental constituents of all living beings. They participate in energy metabolism, account for the assembly of biological membranes, act as signaling molecules, and interact with proteins to influence their function and intracellular distribution. Eukaryotic cells produce thousands of different lipids, each endowed with peculiar structural features and contributing to specific biological functions. With the development of lipidomics, we can now understand the lipid compositional complexity of cells and start making sense of lipidome dynamics. Lipidomes indeed vary among cell types and are reprogrammed in differentiation events. However, whether and how lipidome remodeling assists changes in cell identity is not understood.

RATIONALE: Human dermal fibroblasts are cell constituents of our skin that display cell-to-cell phenotypic heterogeneity as a result of their dynamic cell identity. Thus, individual dermal fibroblasts can adopt different cell specializations that are responsible for wound repair, fibrosis, or remodeling of the extracellular matrix. Whether lipid metabolism is differently shaped in fibroblasts with different phenotypes and if lipid composition participates in the establishment of fibroblast subtypes were unknown. Here, we addressed both the overall lipid composition and phenotypic states of hundreds of individual dermal fibroblasts looking for a possible role of lipids in the determination of dermal fibroblast identity.

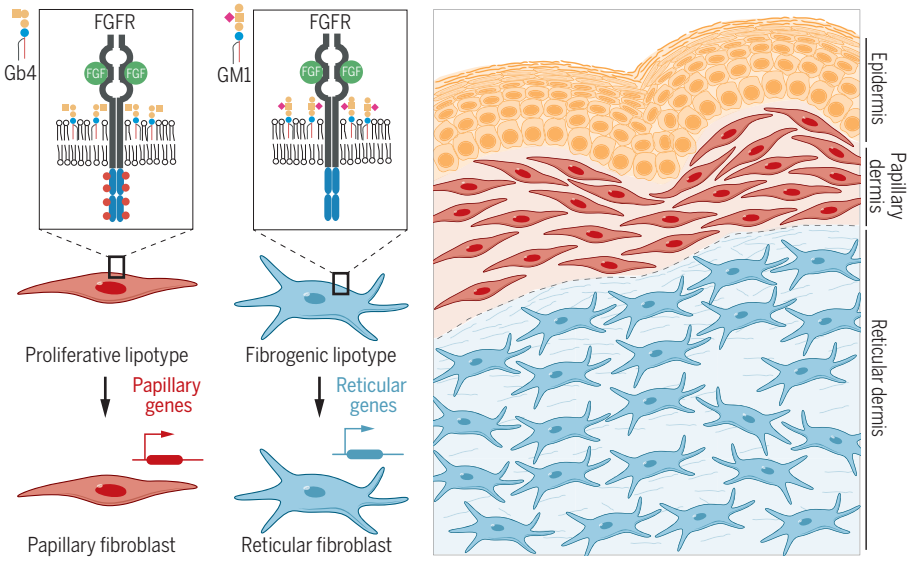

Sphingolipids control dermal fibroblast heterogeneity. Human dermal fibroblasts exist in multiple lipid configurations (lipotypes) marked by different sphingolipids. Sphingolipids such as Gb4 or GM1, distinctly modulate FGF receptor (FGFR) signaling upon exposure to FGF2. As a result of this modulation, lipotypes promote alternative transcriptional programs that are associated with papillary or reticular fibroblasts. Accordingly, fibroblasts bearing different lipotypes populate the reticular and papillary layers of the skin.

RESULTS: We coupled high-resolution mass spectrometry imaging and single-cell mRNA sequencing to resolve both lipidomes and transcriptomes of individual dermal fibroblasts. We found that dermal fibroblasts exist in multiple lipid compositional states that correspond to transcriptional subpopulations in vitro and to fibroblasts populating different layers of the skin in vivo. We isolated the metabolic pathways that account for this correlation and found that sphingolipids are major markers of the different lipid compositional states that we named lipotypes. We also found that lipotype heterogeneity influences cell identity by diversifying the response of otherwise identical cells to extracellular stimuli and that manipulating sphingolipid composition is sufficient to reprogram cells toward different phenotypic states. We also found that lipid composition and signaling pathways are wired in self-sustained circuits that account for the metabolic and transcriptional fibroblast heterogeneity. Specifically, we observed that sphingolipids modulate fibroblast growth factor 2 (FGF2) signaling, with globo-series sphingolipids acting as positive regulators and ganglio-series glycosphingolipids as negative regulators. In turn, FGF2 signaling counteracts ganglioside production by sustaining the alternative metabolic pathway leading to the production of globo-series sphingolipids.

CONCLUSION: By studying the lipid composition of individual cells, we found that lipids play a driving role in the determination of cell states. We indeed uncovered an unexpected relationship between lipidomes and transcriptomes in individual cells. In fact, our results indicate that the acquisition of specific lipotypes influenced the activity of signaling receptors and fostered alternative transcriptional states. Cell states are intermediates in the process of cell differentiation in which state switches precede terminal commitment. As a consequence, lipidome remodeling could work as an early driver in the establishment of cell identity, and following lipid metabolic trajectories of individual cells could have the potential to inform us about key mechanisms of cell fate decision. Thus, this study stimulates new questions about the role of lipids in cell-fate decisions and adds a new regulatory component to the self-organization of multicellular systems. ■

The list of author affiliations is available in the full article online.
*Corresponding author. Email: gioele.lamanno@epfl.ch (G.L.M.); giovanni.dangelo@epfl.ch (G.D.)
Cite this article as L. Capolupo *et al.*, *Science* **376**, eabh1623 (2022). DOI: 10.1126/science.abh1623

READ THE FULL ARTICLE AT
https://doi.org/10.1126/science.abh1623

RESEARCH ARTICLE

LIPIDOMICS

Sphingolipids control dermal fibroblast heterogeneity

Laura Capolupo[1], Irina Khven[2], Alex R. Lederer[2], Luigi Mazzeo[3], Galina Glousker[4], Sylvia Ho[1], Francesco Russo[5], Jonathan Paz Montoya[1], Dhaka R. Bhandari[6], Andrew P. Bowman[7], Shane R. Ellis[7,8,9], Romain Guiet[10], Olivier Burri[10], Johanna Detzner[11], Johannes Muthing[11], Krisztian Homicsko[12,13,14], François Kuonen[15], Michel Gilliet[15], Bernhard Spengler[6], Ron M. A. Heeren[7], G. Paolo Dotto[16,17,18], Gioele La Manno[2]*, Giovanni D'Angelo[1,5]*

Human cells produce thousands of lipids that change during cell differentiation and can vary across individual cells of the same type. However, we are only starting to characterize the function of these cell-to-cell differences in lipid composition. Here, we measured the lipidomes and transcriptomes of individual human dermal fibroblasts by coupling high-resolution mass spectrometry imaging with single-cell transcriptomics. We found that the cell-to-cell variations of specific lipid metabolic pathways contribute to the establishment of cell states involved in the organization of skin architecture. Sphingolipid composition is shown to define fibroblast subpopulations, with sphingolipid metabolic rewiring driving cell-state transitions. Therefore, cell-to-cell lipid heterogeneity affects the determination of cell states, adding a new regulatory component to the self-organization of multicellular systems.

The division of labor is a fundamental organizational principle of multicellular organisms that is implemented through transcriptional programs resulting in cell types. However, phenotypic heterogeneity can occur across cells of the same type, resulting in different cell states (*1*–*3*). These varying cell states can have physiological significance such as priming diverging differentiation programs (*4*) or contributing to distinct cellular tasks in physiological processes (*5*).

Fibroblasts are a cell type that can plastically transition across multiple states (*6*–*13*). Changes in the proportion of fibroblast subpopulations are associated with fibrosis and contribute to a tissue microenvironment permissive for cancer growth (*14*–*18*). Cell lineage, soluble factors, and the microenvironment (*6*) all contribute to the determination of fibroblast states (*15*), yet the molecular circuits that govern this fibroblast heterogeneity and plasticity have not been fully clarified.

Metabolic rewiring is inherent to cell-fate transitions (*19*), and several metabolic switches involving lipids are important for multicellular organism development (*20*). Nonetheless, only a few studies have investigated lipid composition at the single-cell level and the relevance of its variability (*21*–*24*). Thus, whether lipid metabolism has a role in the determination of cell states remains unclear. Specifically, although lipids modulate the differentiation of stem cells in the skin (*25*), whether and how lipid metabolism participates in fibroblast state plasticity has not been addressed.

Mass spectrometry (MS) techniques now have enough sensitivity to enable single-cell lipidomics (*26*–*28*). In particular, matrix-assisted laser desorption/ionization mass spectrometry imaging (MALDI-MSI) provides coverage of the lipid mass-to-charge-number (m/z) range, causes minimal fragmentation, and has reached a spatial resolution compatible with single-cell analysis while maintaining mass resolution and accuracy (*29*–*36*).

MALDI-MSI reveals the organizing principles of lipid heterogeneity

We performed space-resolved (25 to 50 μm^2 pixel size) MALDI-MSI on low-passage primary dermal human fibroblasts (dHFs) (Fig. 1A). Lipid images (Fig. 1B) were extracted from raw data and lipid identity was attributed (*37*) and validated by electrospray ionization liquid chromatography–mass spectrometry (ESI-LC/MS) (*37*) and multiple reaction monitoring (MRM)–based lipidomics (Fig. 1A; fig S1, A and B; and table S1). Specific attributions were disambiguated by comparison with pure standards (fig. S1C) and targeted LC-MS/MS (fig. S1D). Overall, images of 205 annotated lipids were obtained (*37*) (table S1), which account for a sizable fraction of the dHF lipidome as detected by LC-MS.

The intensities of all the m/z peaks at each scanned location (i.e., pixel) were used to perform a multivariate analysis. Principal component analysis (PCA) revealed that 95% of the pixel-to-pixel variability could be explained by eight principal components (PCs) (Fig. 1C and fig. S1E). The in situ visualization of the PC coordinates corresponding to each pixel delineated distinct distribution patterns for different groups of lipids (Fig. 1C).

PC1 coordinates changed from the inner part of the cell toward the cell periphery, suggesting that this axis captures fundamental differences in lipid composition of the perinuclear and peripheral cell membranes (Fig. 1D). In contrast to what was observed for PC1, PC2 to PC8 coordinates distributed differently among cells, with some cells displaying exclusively positive or negative pixels (Fig. 1C). Lipids belonging to the sphingolipid pathway [i.e., ceramides (Cers), sphingomyelins (SMs), hexosylceramides (HexCers), trihexosylceramides (Gb3s), and globosides (Gb4s)] accounted for these axes of cell-to-cell variation (Fig. 1D and fig. S1E). This confirms previous observations concerning the cell-to-cell variability of specific sphingolipids (*21*, *24*) and extends them to most of the lipid species observed in this pathway. From these results, we conclude that two coexisting axes of lipid variation exist in dHFs. One axis pertains to intracellular organization (*38*) and the other to lipid-related intercellular heterogeneity (*39*).

Single-cell analysis reveals lipid coregulation

To understand the nature of this lipid intercellular heterogeneity, we used optical images to guide cell segmentation and transferred them onto the MS images to obtain a total of 257 single-cell lipidomes from three independent MALDI-MSI recordings (Fig. 2A). After data normalization and batch correction, the cell-to-cell variability associated with individual lipid species was summarized by computing their coefficient of variation (CV) (*37*) across the cell population. The obtained values were used to rank lipids according to their

[1]Interfaculty Institute of Bioengineering and Global Health Institute, École Polytechnique Fédérale de Lausanne, CH-1015 Lausanne, Switzerland. [2]Brain Mind Institute, Faculty of Life Sciences, École Polytechnique Fédérale de Lausanne, CH-1015 Lausanne, Switzerland. [3]Department of Biochemistry, University of Lausanne, CH-1066 Epalinges, Switzerland. [4]School of Life Sciences, Swiss Institute for Experimental Cancer Research, École Polytechnique Fédérale de Lausanne, CH-1015 Lausanne, Switzerland. [5]Institute of Biochemistry and Cellular Biology, National Research Council of Italy, 80131 Napoli, Italy. [6]Institute for Inorganic and Analytical Chemistry, Justus Liebig University Giessen, 35392 Giessen, Germany. [7]Maastricht MultiModal Molecular Imaging Institute, Division of Imaging Mass Spectrometry, Maastricht University, 6629 ER Maastricht, Netherlands. [8]Molecular Horizons and School of Chemistry and Molecular Bioscience, University of Wollongong, Wollongong, New South Wales 2522, Australia. [9]Illawarra Health and Medical Research Institute, Wollongong, New South Wales 2522, Australia. [10]Faculté des Sciences de la Vie, Bioimaging and Optics Platform, École Polytechnique Fédérale de Lausanne, Lausanne, CH-1015 Vaud, Switzerland. [11]Institute of Hygiene, University of Münster, D-48149 Münster, Germany. [12]Department of Oncology, Centre Hospitalier Universitaire Vaudois, CH-1011 Lausanne, Switzerland. [13]Swiss Cancer Center Leman, CH-1015 Lausanne, Switzerland. [14]The Ludwig Institute for Cancer Research, Lausanne Branch, CH-1066 Epalinges, Switzerland. [15]Département de Dermatologie et Vénéréologie, Centre Hospitalier Universitaire Vaudois, CH-1011 Lausanne, Switzerland. [16]Personalized Cancer Prevention Research Unit, Head and Neck Surgery Division, Centre Hospitalier Universitaire Vaudois, CH-1011 Lausanne, Switzerland. [17]Department of Biochemistry, University of Lausanne, CH-1066 Epalinges, Switzerland. [18]Cutaneous Biology Research Center, Massachusetts General Hospital, Charlestown, MA 02129, USA.
*Corresponding author. Email: gioele.lamanno@epfl.ch (G.L.M.); giovanni.dangelo@epfl.ch (G.D.)

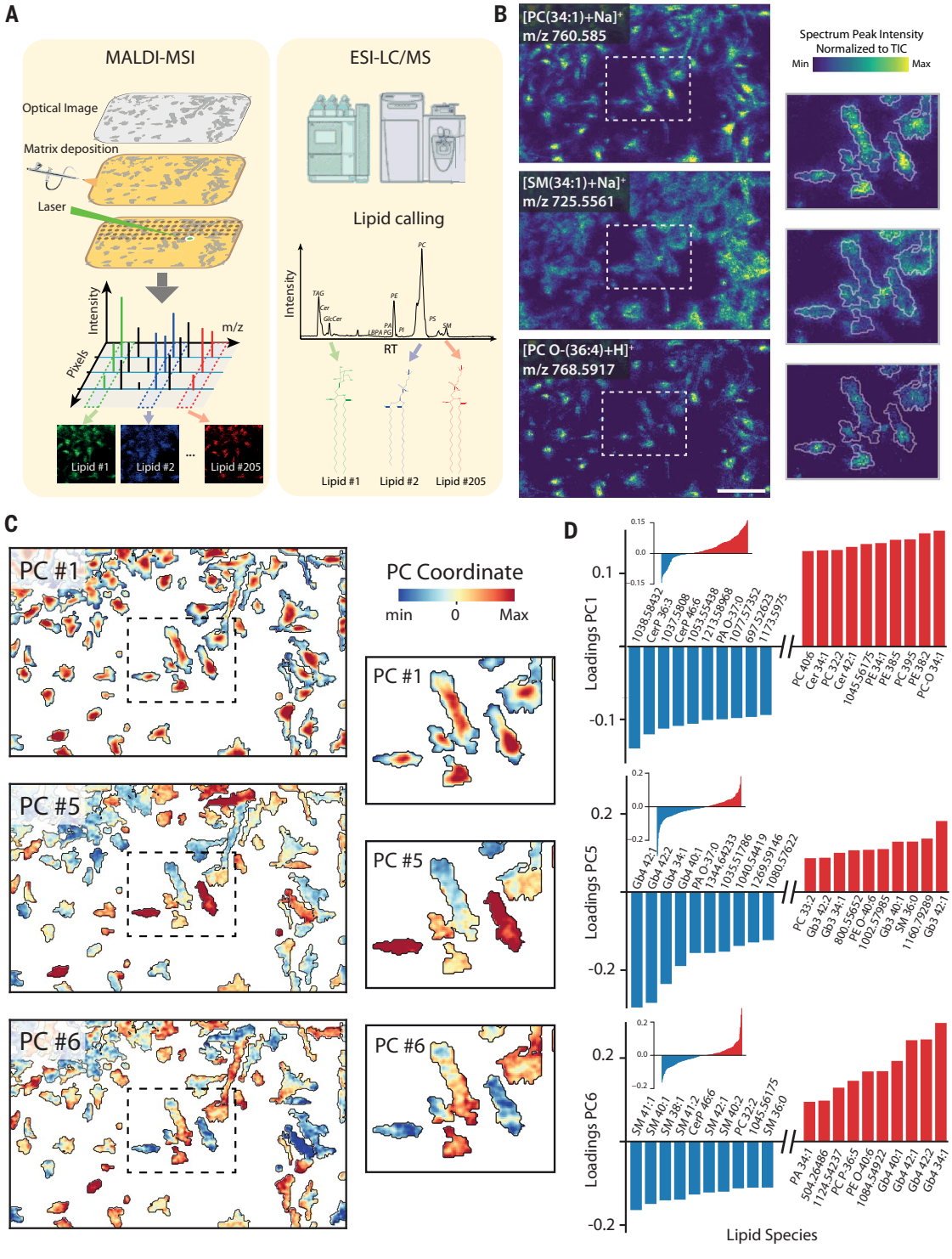

Fig. 1. Single-pixel MALDI-MSI analysis on dHFs. (**A**) Schematic drawing of MALDI-MSI workflow. Cells were fixed, matrix was deposited, and MALDI-MSI was performed by rasterizing the laser across a selected area. For each spot, a mass spectrum was collected and mass images were obtained for each ion by plotting *m/z* intensity at the corresponding *x* and *y* coordinates (left panel). For peak identification, total lipid extracts were analyzed by ESI-LC/MS (right panel). Lipids identified by ESI-LC/MS were then compared with the ones obtained by MALDI-MSI. (**B**) Ion images (50 μm^2/pixel; 354 × 218 pixels) of selected lipids recorded in positive-ion mode. Insets show individual cells images at higher magnification. $[PC(34:1)+Na]^+$, phosphatidylcholine with acyl chains consisting of 34 carbon atoms and one double bond complexed with sodium; $[SM(34:1)+Na]^+$, SM with a backbone of 34 carbon atoms and one double bond complexed with sodium; $[PC\ O\text{-}(36:4)+H]^+$, phosphatidylcholine plasmalogen with acyl chains consisting of 36 carbon atoms and four double bonds complexed with hydrogen; TIC, total ion current. Scale bar, 500 µm. (**C**) Images displaying at each location the PCA coordinate of each pixel. PC1, PC5, and PC6 values are displayed using a divergent color map; positive coordinates are shown in red and negative in blue. Insets show individual cell images at higher magnification. (**D**) Bar plots showing the contribution of the top 10 lipids with higher (red) and lower (blue) loadings for each PC. Miniatures in the upper left corner show the entire distribution.

decreasing CV. Sphingolipids populated the top CV ranking positions, confirming that the sphingolipid pathway (fig. S1F) is subjected to high cell-to-cell variability (Fig. 2B).

To test whether the sphingolipid metabolic pathway is coordinately modulated or if different sphingolipid subsets are controlled independently in different cells, we created a pairwise lipid-lipid correlation (Pearson's *R*) matrix (Fig. 2C). Although phospholipid species did not form biochemically meaningful cliques, sphingolipids were clustered in groups consisting of compounds bearing the same head group (i.e., OH with Cers, hexose with HexCers, trihexose with Gb3s, and *N*-acetyl-hexose-trihexose with Gb4s) but with different Cer backbones (mostly 34:1, 40:1, 42:1, and 42:2) (fig. S1F). This suggests that specific enzymatic

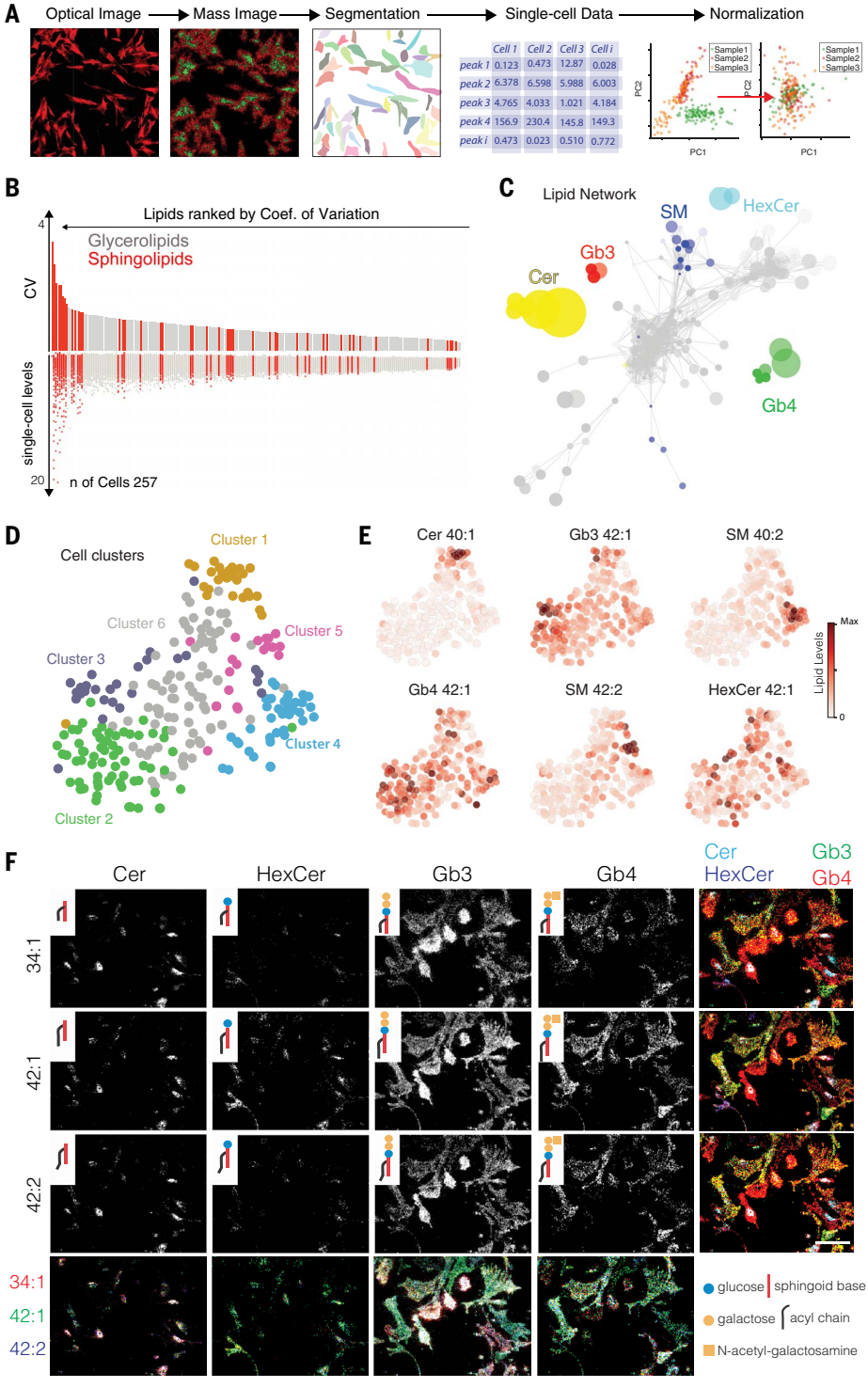

Fig. 2. Single-cell lipidomics analysis. (**A**) Schematic of the approach used for single-cell analysis of MALDI-MSI data. Confocal micrographs were used as guides to segment cells out of the mass images, and single-cell ion abundance was computed as the TIC-normalized peak intensity. Different acquisitions were combined after ComBat batch correction. (**B**) Barplot showing the CV of lipids computed across 257 cells. Lipids were ranked by CV and color coded according to their class (sphingolipids are shown in red, glycerolipids in gray). Single-cell lipid levels are shown in the bottom part of the plot. (**C**) Lipid covariation network. Nodes represent individual lipids, size is proportional to the CV, and color is according to lipid class: Cers are shown in yellow, Gb3s in red, SMs in blue, HexCers in cyan, and Gb4s in green. Edges connect two lipids where the correlation coefficient is >0.85. (**D**) t-distributed stochastic neighbor embedding (t-SNE) of the single-cell lipidomics data. Cells are colored by the clusters defined by hierarchical clustering. (**E**) t-SNE colored by the abundance of sphingolipids. (**F**) Mass images showing the spatial distribution of sphingolipid precursors (Cers and HexCers) and complex sphingolipids (Gb3s and Gb4s) composed of different backbones (34:1, 42:1, and 42:2). Miniatures in the top left corner of each image depict a simplified schematic of the lipid structure (compare with fig. S2A). Scale bar, 500 μm.

activities responsible for Cer processing, rather than those producing different Cer backbones, are variable at a cell-to-cell level. Accordingly, the relative abundances of lipids sharing the same head group were more correlated than those sharing the same backbone (fig. S1G).

Single-cell lipidomes were then used to group cells according to their lipid composition (*37*), resulting in distinct cell clusters (Fig. 2D and fig. S1H). When the levels of sphingolipids were considered, we observed that certain species (i.e., Cers, HexCers, Gb3s, and Gb4s) were enriched in specific cell clusters, suggesting that dHFs exist in distinct sphingolipid metabolic states (Fig. 2, E and F).

Sphingolipids define dHF lipotypes

To validate these results, we stained cells with fluorescently labeled bacterial toxins that recognize different sphingolipid head groups: Shiga toxin 1a (ShTxB1a) binds to Gb3 (*40*), Shiga toxin 2e (ShTxB2e) binds to Gb3 and Gb4 (*41*), and Cholera toxin B (ChTxB) binds the ganglioside GM1 (*42*). Toxins stained dHFs with a pattern reminiscent of the variability observed by MALDI-MSI (Fig. 3A and fig. S2A). Treatment with inhibitors of sphingolipid production [fumonisin B1 (FB1) (*43*) and D-threo-1-phenyl-2-decanoylamino-3-morpholino-1-propanol (D-PDMP) (*44*)] or silencing the expression of

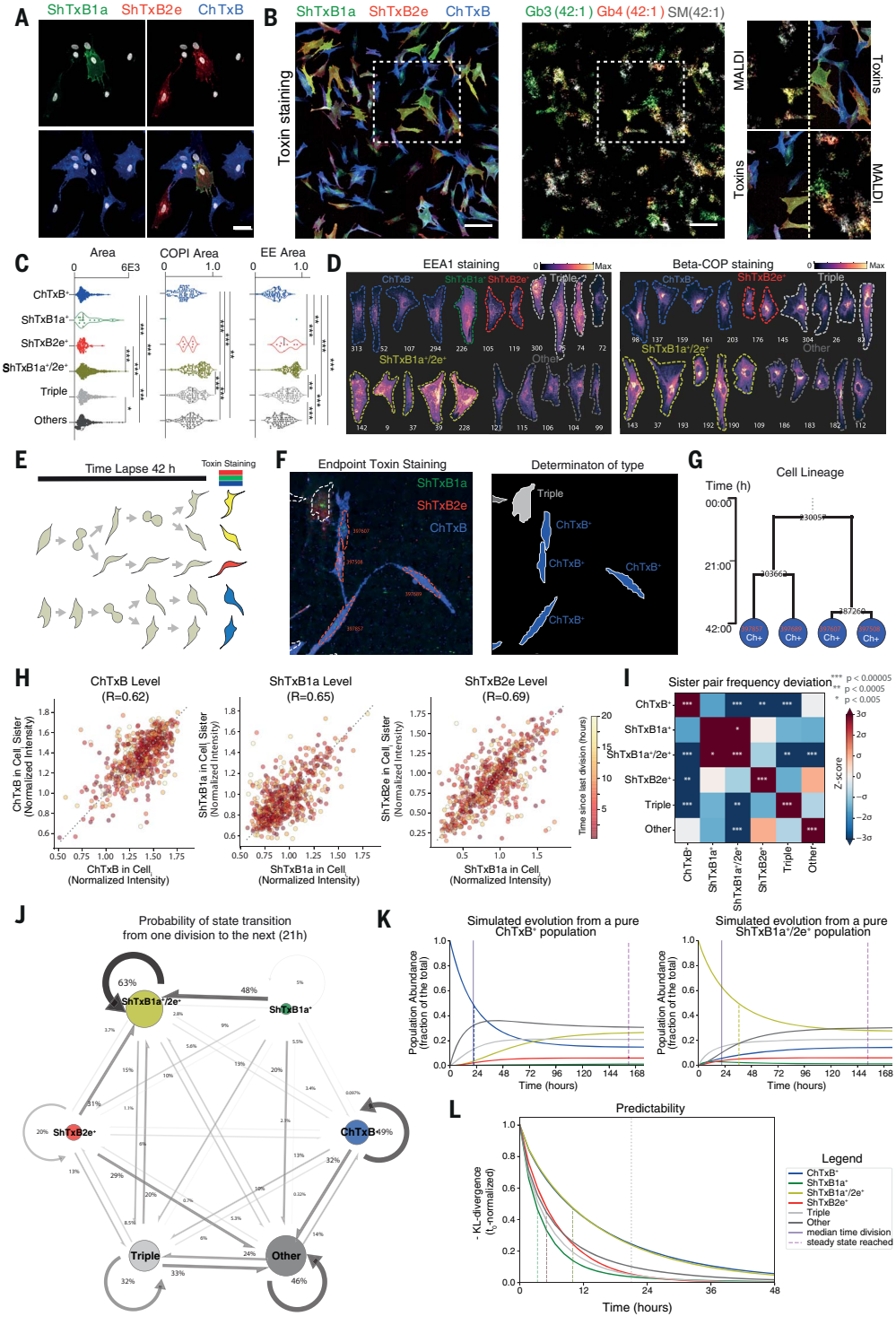

Fig. 3. Identification of dHF lipotypes by MALDI-MSI and toxin staining. (**A**) Confocal micrographs showing cells stained with bacterial toxins ShTxB1a (green), ShTxB2e (red), ChTxB (blue), and Hoechst (gray) for nuclei. Scale bar, 50 μm. (**B**) Side-by-side comparison of toxin staining and MALDI-MSI acquisition on the same cells. First, cells were stained with bacterial toxins as in (A), and images were acquired by confocal microscopy (left panel). Then, MALDI-MSI (25 μm^2/pixel) was performed on the same cells (center panel). Mass images (320 × 320 pixels) of complex sphingolipids [SM (42:1), Gb3 (42:1), and Gb4 (42:1)] are shown. Scale bar, 200 μm. (**C**) Cells were stained with bacterial toxins as in (A) and with antibodies against Beta-COP (COPI vesicles) or EEA1 [early endosomes (EEs)], and images were acquired by confocal microscopy. Normalized fluorescence intensities of toxin and organelle marker stainings of single cells were used to analyze the correlation between lipotypes and cell area and with exo/endocytic organelles. Data are shown as violin plots. *P < 0.05, **P < 0.01, ***P < 0.001, ordinary one-way ANOVA. (**D**) Representative cells stained as for EEA1 or Beta-COP and classified according to their lipotypes. (**E**) Schematic representation of dHF cell lineage tracking. (**F**) Representative confocal micrograph of toxin-stained dHFs before (left) and after (right) segmentation with Cellpose. Segmented cell colors correspond to the different lipotypes. (**G**) Lineage reconstruction for the cells illustrated in (F) as inferred using TrackMate (*37*). (**H**) Correlation plots of normalized ChTxB, ShTxB1a, and ShTxB2e intensities between daughter cells at the time course end point. Dots are colored by the number of hours after mother cell division. (**I**) Heatmap of frequencies for two lipotypes occurring in two sister cells colored by z-score. Positive deviation from zero indicates an increased observed frequency of the sister-lipotype combination compared with random chance, and negative deviation from zero indicates a decreased observed frequency of the sister-lipotype combination compared with random chance. P values were calculated using the bootstrap pairwise t test (*37*). (**J**) Probability of a lipotype state transition occurring in a cell over a 21-hour time period as estimated using CELLMA (*37*). Probabilities are located at the corresponding arrow tails. (**K**) Markov model–simulated evolution of a pure ChTxB$^+$ (left) or pure ShTxB1a$^+$/2e$^+$ (right) cell population over 7 days. (**L**) Line plots displaying the evolution of the state predictability of a cell (or its progeny) after a certain time from an original state measurement. Differently colored tracks correspond to a different original lipotype measurement (t = 0). Kullback-Leibler divergence is evaluated between the probability distribution vector obtained using the Markov transition matrix and the steady-state probability distribution (i.e., the best uninformed guess).

B4GALT5 encoding lactosylceramide synthase (LCS) reduced toxin binding (fig. S2, B and C) without inducing significant toxicity (fig. S2D), indicating that toxins are a faithful proxy for dHF sphingolipid composition in our setting.

As further validation, dHFs were first fixed and stained with toxins and then imaged by MALDI-MSI (Fig. 3B). ShTxB1a staining correlated best with Gb3 levels, and ShTxB2e staining correlated well with Gb3 and Gb4 levels, whereas neither correlated with SM levels. ChTxB staining, our proxy for the levels of GM1 (*42*), a sphingolipid not detected by MALDI-MSI in positive-ion mode, did not correlate with any of the sphingolipids detected

by mass imaging (fig. S2, E and F). We then analyzed dHFs derived from four unrelated healthy individuals that displayed an analogous pattern of cell-to-cell sphingolipid variability (fig. S2G), suggesting that bacterial toxins capture cell-to-cell sphingolipid heterogeneity and that sphingolipid heterogeneity is common to dHFs from different individuals.

We categorized dHFs depending on their sphingolipid configurations into ChTxB$^+$, ShTxB1a$^+$, ShTxB2e$^+$, ShTxB1a$^+$/2e$^+$, triple$^+$, and "other" (accounting for all other configurations) (fig. S3A). When looking at features associated with these categories (Fig. 3C and fig. S3B), we observed that ShTxB1a$^+$/2e$^+$ and triple$^+$ cells were larger than ChTxB$^+$ and ShTxB2e$^+$ cells and that ShTxB1a$^+$/2e$^+$ had a more complex shape than ChTxB$^+$ cells (Fig. 3C and fig. S3B). We also considered the cell-to-cell variability associated with exo/endocytic organelles (*45*), where sphingolipid production and turnover take place (*46*). We observed that ShTxB1a$^+$/2e$^+$ dHFs have an expanded early endosomal compartment compared with other configurations, with ChTxB$^+$ dHFs showing an opposite phenotype. Similar, although less striking, changes were observed when looking at coat protein complex I (COPI) vesicles and at the Golgi complex (Fig. 3, C and, D, and fig. S3, C and D). Thus, dHFs exist in different lipid metabolic configurations that correspond to distinct cell phenotypes involving cell size and shape and are endowed with different endocytic and secretory states.

To assess the dynamics of sphingolipid configurations, dHF lineages were followed by live microscopy, and individual cells were analyzed by toxin staining after fixation (Fig. 3, E to G; fig. S4A; and movie S1). When the intensity levels associated with individual toxins were considered in pairs of sister cells, we noticed that they were correlated (Fig. 3H) and that lineage-related cells had a higher probability of sharing the same sphingolipid configuration than would be expected by chance (Fig. 3I and fig. S4, B to D). Considering the toxin-staining patterns of lineage-related cells, we modeled the dynamics of lipid configuration switches by developing the cell-state transition estimation by lineage leaf-state Markov analysis (CELLMA) algorithm (*37*). This model predicted that ShTxB1a$^+$/2e$^+$, ChTxB$^+$, and triple$^+$ are stable states with a 37%, 51%, and 68% probability of converting into a different lipid configuration during a single-cell replication cycle (21 hours), respectively. Conversely, ShtxB1a$^+$ and ShtxB2e$^+$ states were more transient and showed a greater propensity (95 and 80% during a single replication, respectively) for converting into ShTxB1a$^+$/2e$^+$ or into "other" lipid configurations (Fig. 3J and fig. S4E).

These dynamics translate into lipid-state transition fluxes such that the predominant lipid configurations are propagated across cell generations (fig. S4F). Accordingly, our model predicts that populations composed of cells all belonging to the same lipid category would revert slowly (i.e., within 7 days) to a heterogeneous steady state (Fig. 3K and fig. S4G). In agreement with this prediction, when we selected ShTxB1a$^+$ or ChTxB$^+$ cells by fluorescence-activated cell sorting (FACS) and kept them in culture for 10 days, the cell cultures reverted to heterogeneous cell populations with lipid-state compositions similar to those from which they were originally selected (fig. S4H).

On the basis of these results, we conclude that dHFs exist in metastable sphingolipid metabolic configurations (Fig. 3L) that correspond to given phenotypic states and persist during cell generations. Hereafter, we refer to these lipid metabolic states as lipotypes.

Lipotypes mark specific cell transcriptional states

We performed single-cell RNA sequencing (scRNA-seq) on a total of 5652 dHFs. Uniform manifold approximation and projection (UMAP) embedding was computed on the gene expression profiles, and 17 cell clusters were identified by the Louvain algorithm (Fig. 4A). These 17 clusters were grouped into six categories related to different biological processes: proliferation, proinflammatory cytokine secretion (inflammatory), profibrotic secretion (fibrogenic), extracellular matrix remodeling (fibrolytic), and proangiogenic factor secretion (vascular) (Fig. 4B and fig. S5A). A further group represented bona fide basal-state fibroblasts (basal). We investigated the dynamic relationships among these categories using diffusion maps (*47*) and partition-based graph abstraction (PAGA), which estimate the trajectories and connectivity of the different components of a manifold (*48*). This analysis revealed that basal and proliferating categories were interconnected, whereas inflammatory, fibrogenic, and fibrolytic categories represented mutually alternative transcriptional cell configurations (Fig. 4, C and D).

Next, to link the expression-defined subtypes with those defined by sphingolipids, we isolated dHFs according to their lipotypes by FACS and performed bulk RNA sequencing on the different sorted samples. We isolated ChTxB$^+$, ShTxB2e$^+$, ShTxB1a$^+$/2e$^+$, and triple$^+$ cells (Fig. 4E and fig. S5B). Genes up-regulated in the different lipotypes were extracted and used to compute gene signature scores on the single-cell dataset. The four lipotype signatures mapped to distinct UMAP areas that corresponded to the major transcriptional categories (Fig. 4, F and G). Triple$^+$ cells corresponded to inflammatory, fibrolytic, and vascular fibroblasts; ShTxB1a$^+$/2e$^+$ and ShTxB2e$^+$ to proliferating cells and basal state fibroblasts; and ChTxB$^+$ to "fibrogenic" fibroblasts. This suggests that specific lipotypes are associated with prevalent cell states (Fig. 4H). To verify this finding, we costained dHFs with toxins and markers for the different clusters, which revealed a specific overlap between ChTxB and smooth muscle actin (encoded by the gene *ACTA2*, a fibrogenic marker)–positive cells and between ShTxB2e and laminin A (encoded by the gene *LMNA*, a basal and proliferative marker)–positive cells. Altogether, these observations indicate that lipotypes are markers of dHF cell states (Fig. 4, I and J).

Lipotypes mark specific dHF populations in vivo

Cell states of dHFs in vitro partly reflect populations of fibroblasts in the skin. Specifically, fibroblasts localized in the deeper dermal region (i.e., reticular fibroblasts) are endowed with fibrogenic activity (*49*), whereas those populating the more superficial region (i.e., papillary fibroblasts) have greater proliferative capability (*50*). Therefore, we derived transcriptional signatures for papillary and reticular dHFs from studies (*51*) and mapped them on our UMAP embedding (Fig. 5A). We found that the reticular signature largely overlaps with the fibrogenic UMAP region (also associated with ChTxB$^+$ signature). Conversely, the papillary signature overlaps with the basal and fibrolytic UMAP regions (also associated with ShTxB2e$^+$ and ShTxB1a$^+$/2e$^+$ signatures) (Fig. 5, A and B).

Accordingly, when we toxin-stained human skin biopsies, we observed that ChTxB$^+$ cells are preferentially found in the reticular dermal region, whereas ShTxB1a$^+$/2e$^+$ cells are prevalently found in the papillary dermal region (Fig. 5C). Counterstaining for the fibroblast marker vimentin and other dermal markers confirmed that dHFs are stained with different specificities by toxins (Fig. 5D and fig. S6). Keratinocytes, as recognized by the marker pankeratin, were primarily ShTxB1a$^+$/2e$^+$ and endothelial cells, as recognized by the marker CD31, were stained by all three toxins (Fig. 5E and fig. S6).

When skin is damaged, for example, from wounding or cancer lesions, dermal fibroblasts become activated and experience phenotypic interconversion (*52*). We stained three skin samples from individuals diagnosed with cutaneous squamous cell carcinoma (cSCC) with sphingolipid-binding toxins. In all three cases, recognizable cancer lesions were surrounded by cells prevalently stained by ChTxB (Fig. 5F and fig. S7, A and B). When counterstained with dermal markers, these ChTxB$^+$ cells were vimentin$^+$, suggesting that they are cancer-associated fibroblasts (CAFs) (fig. S7C).

CAFs can be effectively isolated from cancer tissues. We thus examined two pairs of CAFs and matched dHFs from cSCC and flanking unaffected areas from the same patients (fig. S7, D and E) for toxin analysis. In both cases, CAFs were predominantly ChTxB$^+$ and ShTxB1a$^-$/2e$^-$,

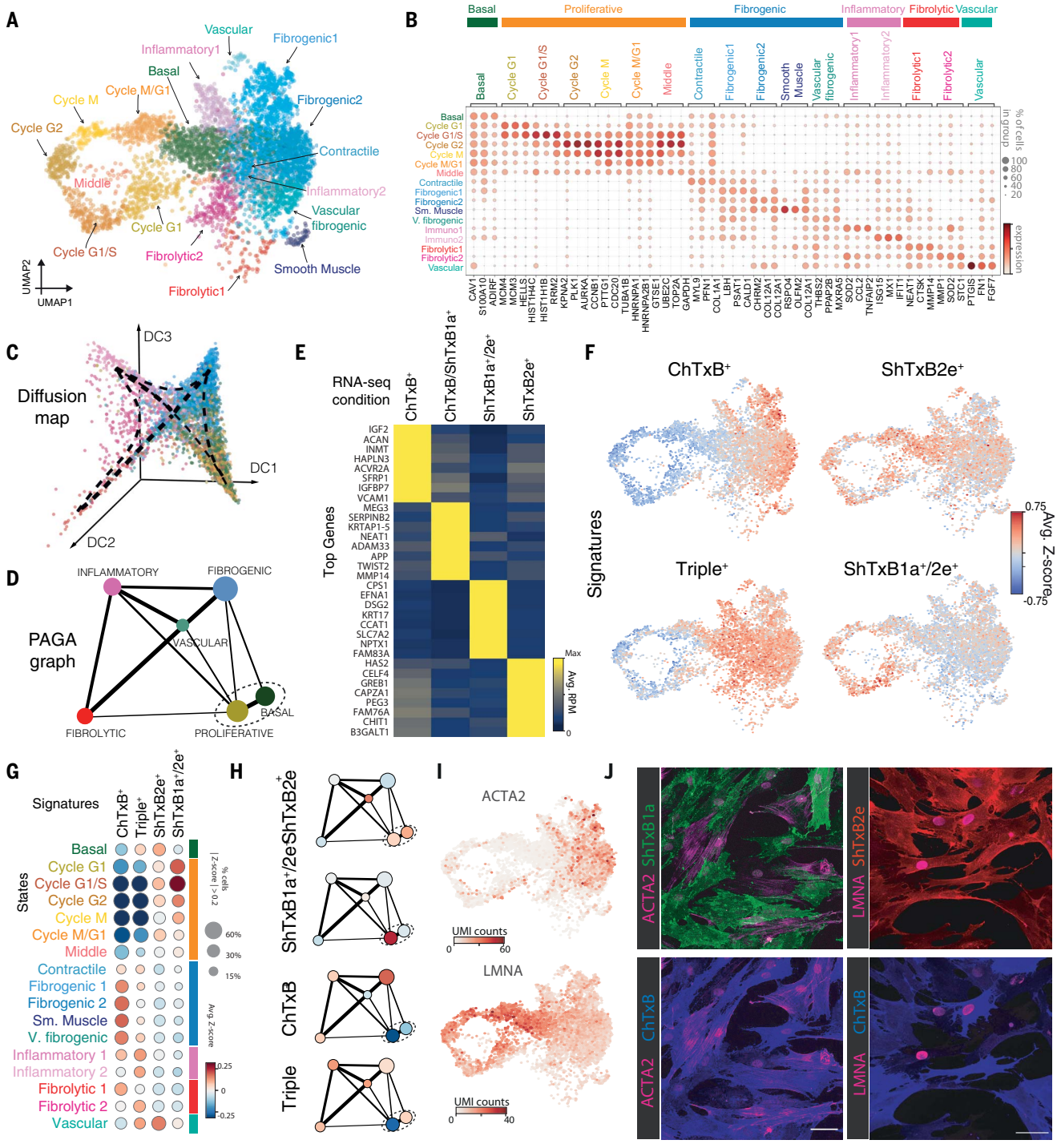

Fig. 4. Lipotype mapping to transcriptional cell states. (**A**) UMAP embedding analysis of scRNA-seq of 5652 individual dHFs colored by the assigned cluster. (**B**) Gene expression dot plot of cluster marker genes. Genes for each cluster were identified using the Wilcoxon rank-sum test. (**C**) Diffusion map visualization of single dHF cells from (A) highlighting the axes of transcriptional variation among the different cell states. (**D**) PAGA applied to scRNA-seq data of control dHFs. Nodes indicate cell type states, and the length of edges indicates the degree of similarity between states, with shorter edges corresponding to greater state similarity. (**E**) Heatmap reporting the average gene expression of enriched genes for each of the FACS-sorted lipotype populations (bulk RNA-seq data). For each lipotype, the top eight genes, ranked by fold change, are shown. (**F**) UMAP embedding colored by the different lipotype gene signature scores. The 250 top differentially expressed genes were used to calculate the signature score. (**G**) Dot plot colored by the average lipotype *z*-score of cells of the different clusters. Size of the dots represents the number of cells with magnitude of the score >0.35. (**H**) PAGA applied to scRNA-seq data of control dHFs and based on the ShTxB2e$^+$, ShTxB1a/2e$^+$, ChTxB$^+$, and triple$^+$ lipotype signatures. Nodes are positioned corresponding to cell states in (D). Color of nodes corresponds to *z*-score signatures, with a positive *z*-score (red) indicating a greater correspondence of the particular cell type to the particular lipotype state. Color bar is the same as in (G). (**I**) UMAP embedding of dHFs colored by the expression of the two canonical markers for fibrogenic (*ACTA2*) and basal (*LMNA*) cell states. (**J**) Confocal micrographs of cells stained with ShTxB1a (green), ShTxB2e (red), and ChTxB (blue) and counterstained by antibodies against ACTA2 and LMNA (magenta). Scale bar, 100 μm.

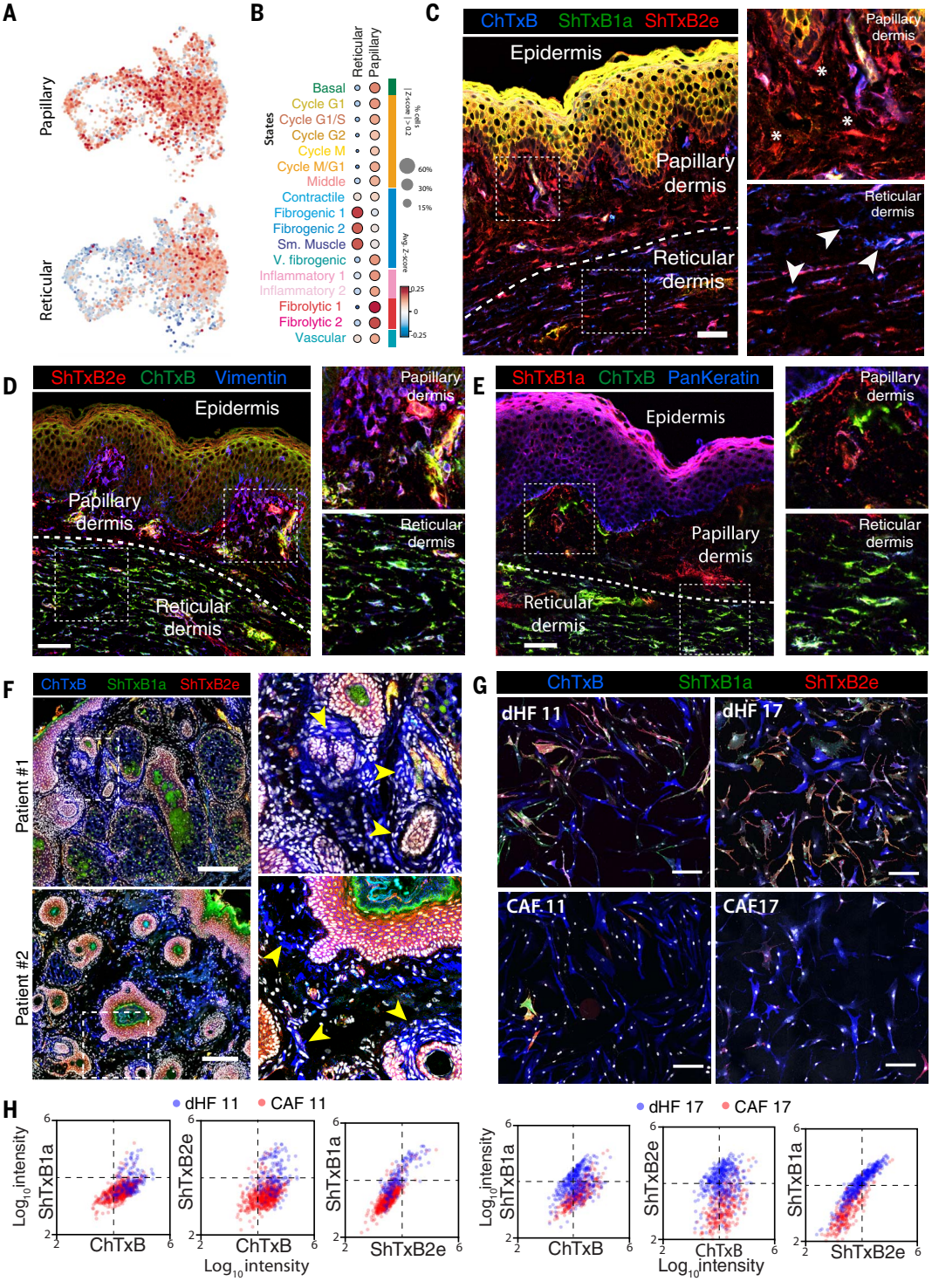

Fig. 5. Lipotypes define dHF population in the skin. (**A**) Papillary and reticular signatures overlaid onto the UMAP embedding. (**B**) Dot plot colored by the average reticular and papillary *z*-score of cells of the different clusters. Size of the dots represents the number of cells with magnitude of the score >0.35. (**C**) Confocal micrographs of human foreskin tissue section stained with bacterial toxins ShTxB1a (green), ShTxB2e (red), and ChTxB (blue). Insets show lipid staining in papillary (asterisks) and reticular (arrowheads) fibroblasts. Scale bar, 200 μm. The dotted line delineates the papillary-reticular dermal boundary. (**D**) Confocal micrographs of human foreskin tissue section stained with bacterial toxins ShTxB2e (red) and ChTxB (green) and vimentin (blue) as a fibroblast marker. Insets show staining in papillary and reticular layers. Scale bar, 200 μm. The dotted line delineates the papillary-reticular dermal boundary. (**E**) Confocal micrographs of human foreskin tissue section stained with bacterial toxins as in (D) and pankeratin (blue) as a keratinocyte marker. Insets show staining in papillary and reticular layers. Scale bar, 200 μm. (**F**) Confocal micrographs of human cSCC sections stained with bacterial toxins as in (C). Scale bar, 200 μm. Insets show tumor regions surrounded by ChTxB$^+$ fibroblasts (yellow arrowheads). (**G**) Confocal micrographs of CAFs and normal dHFs isolated from the same individuals, stained with bacterial toxins as in (C). Scale bar, 200 μm. (**H**) Scatter plots of fluorescence intensity values for each toxin comparing control dHFs (blue) and their corresponding CAFs (red).

compared with matched dHFs (Fig. 5, G and H). These data indicate that dHF lipotypes are reflected by fibroblast subtypes populating different dermal regions and are differently associated with skin cancers.

Sphingolipid composition influences cell states

We surveyed whether lipotypes are the result of cell state–specific transcriptional programs that involve lipid-metabolizing enzymes. Unexpectedly, when the expression of genes encoding sphingolipid enzymes and accessory factors was visualized on the UMAP embedding, none of them showed a cell state–specific localization (fig. S8A). To test this, we combined toxin staining and mRNA fluorescence in situ hybridization (FISH). We assayed the expression of *ST3GAL5* encoding GM3 synthase (GM3S) and *A4GALT* encoding Gb3 synthase (Gb3S) and their lipid products through toxins ChTxB and ShTxB1a within the same cells (Fig. 6A and fig. S8B). When toxin staining intensity was considered along with FISH counts, we observed either no or weak (R = 0.29) correlation of the two readouts, suggesting that single-cell sphingolipid composition is largely determined by posttranscriptional

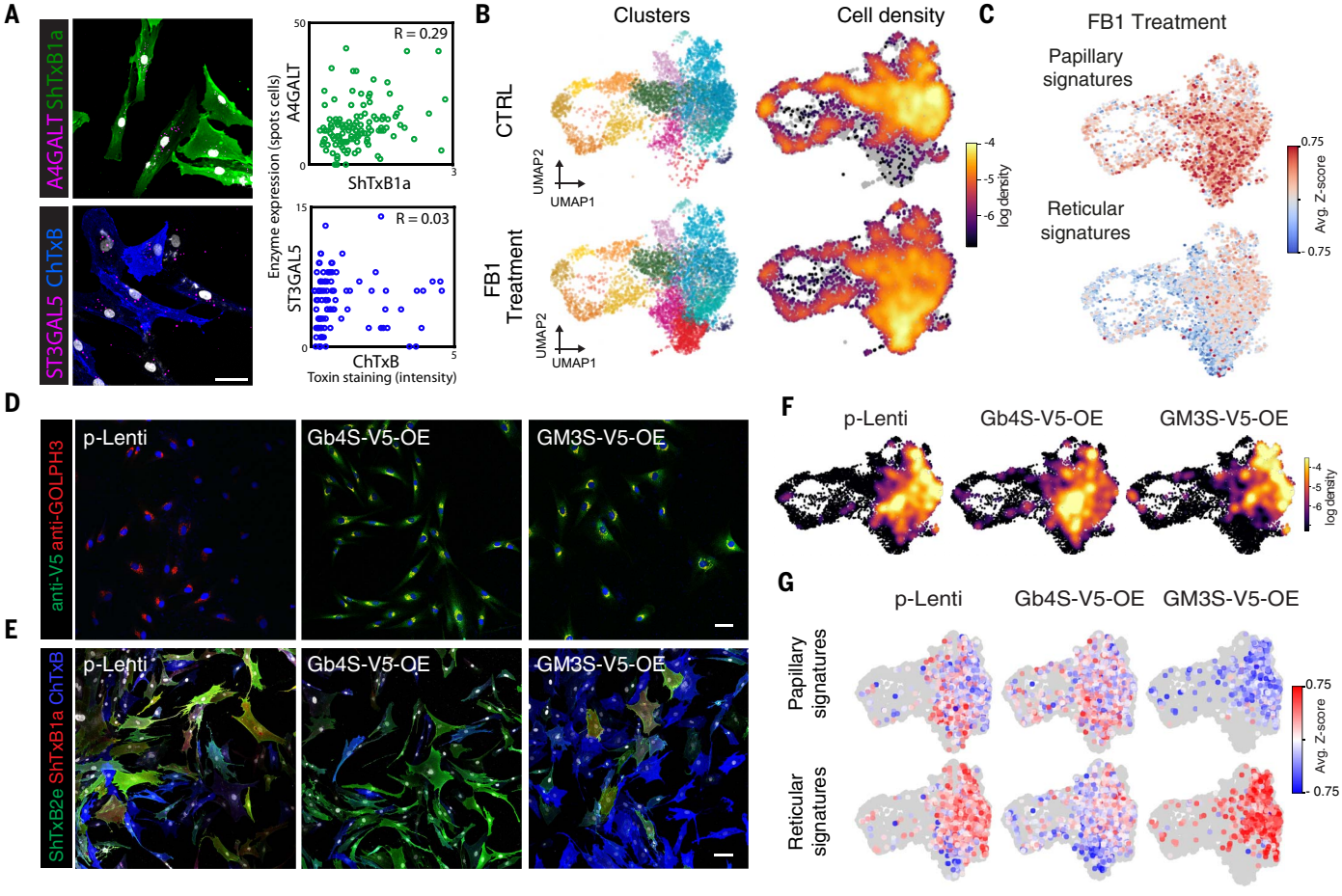

Fig. 6. Effect of sphingolipid perturbations on cell states. (**A**) Representative confocal micrographs of correlative mRNA-FISH/fluorescence toxin staining using *A4GALT* and *ST3GAL5* (magenta) probes and ShTxB1a (green) and ChTxB (blue). Nuclei were labeled with Hoechst (gray). Scale bar, 50 μm. Right, scatterplot showing the level of expression against toxin fluorescence. Pearson's correlation coefficient is indicated. Quantification on 120 and 96 individual cells for *A4GALT* and *ST3GAL5*, respectively. (**B**) Left, UMAP embedding of the scRNA-seq data for the control (5652 individual dHFs) and FB1-treated cells (6546 individual dHFs). Cells are colored by their assigned cluster. Right, density maps of control (CTRL) and FB1-treated cells mapped in the UMAP space. (**C**) Papillary and reticular gene signatures in the FB1-treated sample overlaid onto the UMAP embedding. (**D**) Confocal images of the overexpressing cell lines stained with antibodies against V5 protein tag (green) and GOLPH3 (red). Scale bar, 50 μm. (**E**) Confocal images of the overexpressing cell lines stained with the bacterial toxins ShTxB1a (red), ShTxB2e (green), and ChTxB (blue). Scale bar, 50 μm. (**F**) Cell density plot of single-cell expression profile of the OE dHF cells mapped by similarity onto the UMAP projection in (B). (**G**) Papillary and reticular signatures overlaid onto the UMAP embedding of the OE dHFs.

mechanisms. Therefore, lipotypes are associated with cell states, yet cell states are not endowed with transcriptional programs that would account for the lipotypes with which they are associated. This raises the question of whether lipotypes are causally upstream of cell states and if lipid composition influences cell-to-cell transcriptional heterogeneity.

To test this hypothesis, we treated dHFs with the Cer synthase inhibitor FB1, which blocks the production of sphingolipids (figs. S1F and S2B), and performed scRNA-seq. When FB1-treated dHFs were integrated in the same transcriptional embedding along with control cells, they displayed a different distribution across states (Fig. 6B and fig. S8C). FB1-treated cells were more frequently associated with fibrolytic (from 6% in control cells to 23% in FB1-treated cells) and vascular (from 0.6 to 1.3%) than fibrogenic (from 48 to 40%) and inflammatory (from 9 to 6%; Fig. 6B and fig. S8D) states. These changes correspond to an increased association of FB1-treated dHFs with "papillary" and decreased association with "reticular" fibroblast states (Fig. 6C).

FB1 treatment deprives cells of most sphingolipids (*43*), so this treatment does not inform on how the individual lipid species associated with the cell states influence signaling. We established dHF lines overexpressing either GM3S or Gb4S, two enzymes driving alternative sphingolipid-processing pathways (Fig. 6D). These overexpressing (OE) cells displayed the expected changes in sphingolipid composition, with GM3S-OE dHFs composed largely of ChTxB$^+$ cells and Gb4S-OE dHFs composed largely of ShTxB1a$^+$/2e$^+$ cells (Fig. 6E and fig. S8E).

GM3S-OE and Gb4S-OE lines were then analyzed by scRNA-seq to test the impact of lipotype change on cell state. GM3S-OE and Gb4S-OE dHFs populated two distinct transcriptional regions (Fig. 6F). Gb4S-OE dHFs were more associated with basal, inflammatory, and fibrolytic states, whereas GM3S-OE dHFs were for the major part in a fibrogenic state (88%) and almost never in inflammatory or fibrolytic states (fig. S8F). Gene expression analysis confirmed this transition: *COL12A1* and *VCAN* markers of fibrogenic state were significantly up-regulated in GM3S-OE cells and down-regulated in Gb4S-OE cells, whereas the fibrolytic and inflammatory markers *MMP-1*

and *CCL2* were up-regulated in Gb4S-OE cells and down-regulated in GM3S-OE cells (fig. S8G). Moreover, when reticular and papillary signatures were considered, we found that Gb4S-OE dHFs were clearly more associated with papillary states and GM3S-OE dHFs with reticular states (Fig. 6G).

Sphingolipids integrate into regulatory circuits involved in cell-state determination

The transcriptional changes triggered by FB1 involve targets of fibroblast growth factor 2 (FGF2) activation and of transforming growth factor–β (TGF-β) repression (*53*) (fig. S9A). FGF2 and TGF-β transcriptional programs are in fact largely antagonistic (*53*). Genes up-regulated by FGF2 and down-regulated by TGF-β (such as *MMP-1*) were preferentially expressed in the FB1-treated cells and in the fibrolytic-basal population, whereas genes up-regulated by TGF-β and down-regulated by FGF2 (such as *ACTA2*) were more expressed in control cells and in the fibrogenic population (fig. S9A). This was confirmed by quantitative polymerase chain reaction (qPCR) and immunofluorescence analysis on a panel of selected markers and extended to treatment with D-PDMP and LCS-KD (fig. S9, B to F), suggesting that global sphingolipid deprivation either promotes FGF2 or suppresses TGF-β signaling.

In dHFs challenged with increasing amounts of FGF2 or TGF-β, sphingolipid depletion did not inhibit fibroblast response to TGF-β, whereas it sensitized cells to FGF2 (fig. S9G). Moreover, genetic interruption of FGF signaling through the expression of a dominant-negative version of FGF receptor 1 (DNFGFR1) specifically blunted the transcriptional response to FB1 treatment (Fig. 7, A to C), indicating that transcriptional changes induced by sphingolipid deprivation require FGF signaling.

When FGF2 and TGF-β signatures were mapped onto Gb4S-OE and GM3S-OE dHF UMAPs, we observed that GM3S-OE fostered the TGF-β transcriptional program, whereas for Gb4S-OE, we revealed the opposite trend (fig. S9H). The effect on the FGF2 program was more difficult to observe because the expression signature dominates in actively proliferating cells (fig. S9H). Nonetheless, immunofluorescence experiments showed that although GM3S-OE dHFs were almost uniformly $ACTA2^{+}/MMP1^{-}$, Gb4S-OE dHFs displayed high MMP1 levels (Fig. 7, D and E). This effect was counteracted by the FGF signaling inhibitor infigratinib (fig. S9I), indicating again that transcriptional responses to changes in cellular sphingolipid composition require FGF signaling.

Moreover, stimulating Gb4S-OE and GM3S-OE dHFs with FGF2 resulted in increased and decreased responses, respectively (fig. S9, J and K), and exogenous administration of GM1 to FB1-treated cells (fig. S9L) specifically counteracted MMP1 induction (fig. S9M). This suggests that GM1 and Gb3/Gb4 have opposite modulatory effects on FGF2 signaling. We thus challenged dHFs with FGF2 and monitored the immediate single-cell signaling response by following ERK phosphorylation (*54*) as a function of the cell lipotype. In our conditions, FGF2-induced ERK phosphorylation was maximal after 5 min of stimulation (Fig. 7F and fig. S10A). At this time point, $ShTxB1a^{+}/2e^{+}$ cells displayed a consistently stronger response to FGF2 than $ChTxB^{+}$ cells from the same cell culture dish (Fig. 7G and fig S10, B and C), indicating that dHFs exposing Gb3 and Gb4 at their cell surfaces are more susceptible to FGF pathway activation than those exposing GM1.

Unexpectedly, toxin staining analysis of dHFs in which the FGF2 pathway was blocked either genetically or pharmacologically showed a transition of the dHFs to a $ChTxB^{+}$ state (Fig. 7H and fig. S10, D and E). Along similar lines, FGF2 stimulation induced an increase in the $ShtxB1a^{+}/2e^{+}$ cell population with a concurrent decrease of $ChTxB^{+}$ cells (fig. S10, D and E). This effect was largely nontranscriptional, because in DNFGFR1 dHFs, the production of the Gb3 was reduced as assessed by metabolic labeling (fig. S10F), yet the expression of the genes that encode sphingolipid synthetic enzymes was not modulated (fig. S10G).

Thus, sphingolipids modulate FGF2 signaling, with Gb3/Gb4 acting as positive regulators and GM1 as a negative regulator. In turn, FGF2 signaling counteracts GM1 production by sustaining the alternative metabolic pathway leading to the production of Gb3 and Gb4 (Fig. 7I).

Discussion

Here, we investigated whether and how lipid metabolism affects cell identity by exploring the dHF heterogeneity (*7*, *14*) that results from their plastic interconversion across cell states (*6*, *55*–*57*).

Our observations constitute an example of how cell-to-cell lipid heterogeneity can diversify the processing of extracellular signals and promote cellular responses (*22*). The phenomenon that we describe can be considered an instance of cellular contextual decision-making whereby individual cells route to alternative fates by processing external inputs in the context of their internal states (*58*).

Furthermore, considering both the ubiquity of lipids and their structural diversity, we expect to find other cell types exploiting regulatory strategies analogous to the one that we discovered. By extension, one can hypothesize that lipidome remodeling participates in tissue patterning and organogenesis. If this is correct, then lipid-defined cell states analogous to the lipotypes described here could be involved in developmental symmetry-breaking events and organogenesis (*4*). Indeed, our finding that lipotypes are spatially segregated to different dermal layers in human skin architecture supports this hypothesis.

A limitation of our study is the inability to address lipid and transcriptional trajectories live and in single cells. Although challenging to obtain, time-resolved data have the potential to clarify how lipid metabolic fluxes evolve during cell-state transitions (*59*). We envision that emerging tools such as chemically synthesized lipid probes and live-omics profiling will enable such experiments (*60*, *61*).

In conclusion, by exploiting the potential of space-resolved nontranscriptional single-cell omics, we provide evidence for cell-to-cell heterogeneous lipid metabolism playing an instructive role in the self-organization of multicellular systems.

Methods summary

Human fibroblasts obtained from the dermis of discarded skin samples of circumcised, 1- to 5-year-old healthy males were used for MALDI-MSI analyses. Specifically, samples were analyzed using AP-SMALDI10 or AP-SMALDI5 AF systems using 5- or 7-μm spatial resolution in positive-ion mode in the mass range m/z 400 to 1600. Mass images (n = 296) were then generated and lipids annotated by using a combination of databases, ESI-LC/MS (*62*), and MRM confirmation. To assess lipid variability, single-pixel analysis was performed on the 296 mass images. PCA analysis was performed and the absolute values of the PCA loadings were then used to identify the lipids with the most variance of each single component. Single dHFs were further manually segmented, and raw abundance data for each scan and each pixel in a cell were exported. Normalized lipid count values were used to determine the CV. Pearson's R was used to evaluate lipid and cell covariation.

For lipotype determination and feature extraction, including fluorescence intensities, area, eccentricity, shape complexity, and local cell density, cells were stained with fluorescently labeled B-subunit toxins or primary and secondary antibodies. Cells were then analyzed by confocal microscopy and segmented using Cellpose. Time-lapse imaging coupled with toxin end-point staining was performed to assess the dynamics of lipotype configuration (*63*, *64*). The lineage information extracted from the time-lapse imaging and the cell state from the end-point staining were used to perform a sister-state frequency analysis and to fit the estimation framework CELLMA (*37*, *65*).

To evaluate the association between transcriptional states and lipotypes, scRNA-seq on

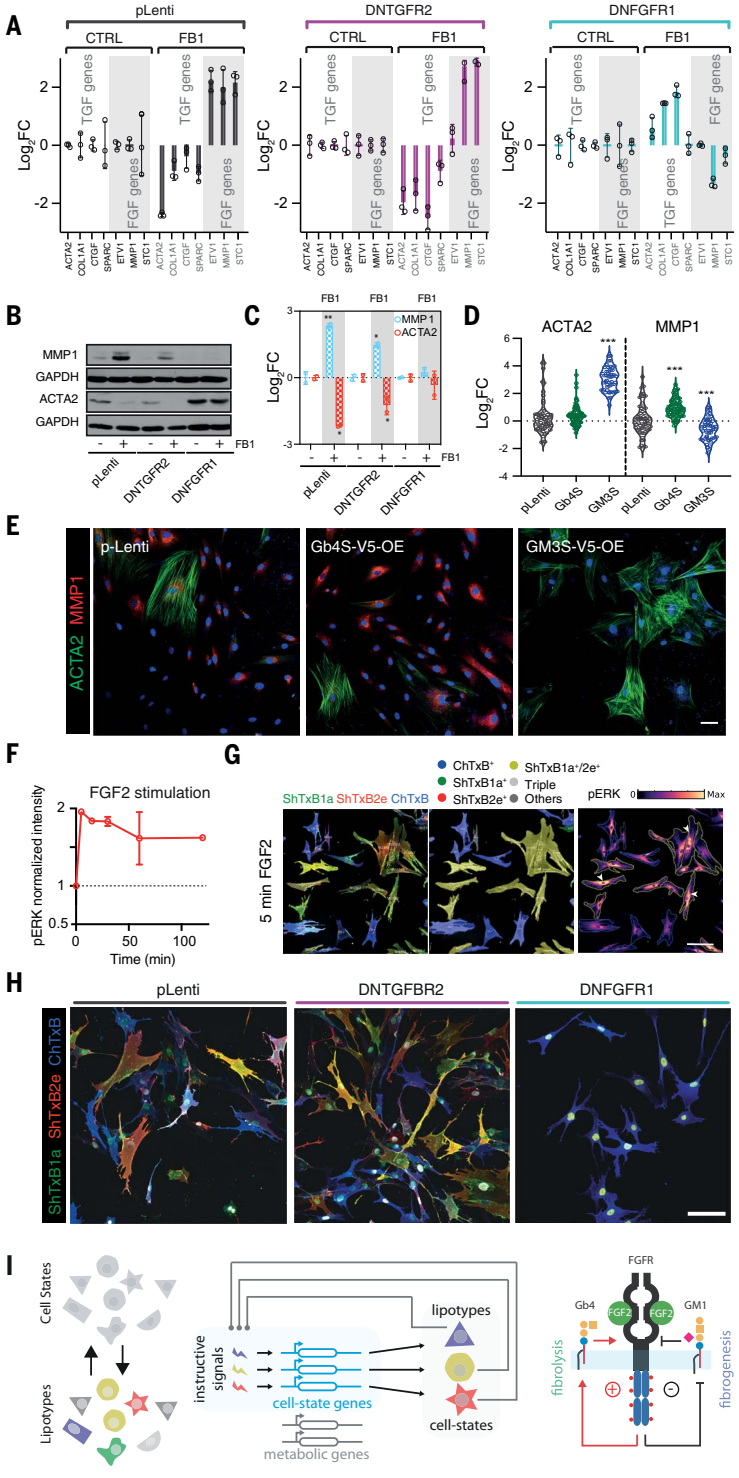

Fig. 7. Effect of sphingolipid perturbation on FGF signaling. (**A**) Barplots of qPCR quantifying the mRNA levels of TGF-β and FGF target genes in CTRL, DNTGFR2, and DNFGFR1 cells treated with 25 μM FB1 for 6 days. Data are shown as log_2-fold change over untreated cells (n = 3; data are shown as means ± SD). (**B** and **C**) Western blot and quantification of cells treated as in (A). Data were normalized against GAPDH (n = 2; data are means ± SD; *P < 0.05, **P < 0.01, Student's t test). (**D**) Cells were stained with ACTA2 and MMP1, and normalized intensity values were extracted for quantification. Data were scaled to the median and are shown as the log_2-fold change over control in an individual cell (CTRL, n = 58; GM3S-OE, n = 49; Gb4S-OE, n = 81; ***P < 0.001, ordinary one-way ANOVA). (**E**) Representative confocal images of OE dHFs stained with antibodies against ACTA2 (green) and MMP1 (red). Scale bar, 100 μm. (**F**) Plots indicating normalized intensity values of pERK protein in cells serum starved and then treated with 5 ng/ml of FGF2 for different times as determined by densitometry. (**G**) Cells treated for 5 min with 5 ng/ml of FGF2 as in (F) were stained with the bacterial toxins ShTxB1a (green), ShTxB2e (red), and ChTxB (blue) (left panel) and pERK (gradient) (right panel). Representative confocal micrographs and cell segmentations according to lipotype are shown. Scale bar, 100 μm. (**H**) Confocal images of pLenti, DNTGFBR2, and DNFGFR1 cells stained with the bacterial toxins ShTxB1a (green), ShTxB2e (red), ChTxB (blue), and Hoechst for nuclei. Scale bar, 100 μm. (**I**) Schematic representation of the model for the role of lipotypes in cell-state determination. Left panel, lipotypes corresponding to dHF cell states. Middle panel, cell states and lipotypes determined by signaling pathways that are in turn influenced by the lipid composition of individual cells. Right panel, FGF2 binds to FGFR, leading to the prevalent production of Gb3/Gb4 over GM1. To close the circuit, GM1 negatively regulates FGFR, whereas Gb3 and Gb4 activate FGFR in a positive feedback loop. This is a bistable system in which cells can be $Gb3^+$ or $Gb4^+$, leading to a more fibrolytic state, or $GM1^+$, leading to a more fibrogenic state.

dHFs and bulk RNA-seq on five cell populations isolated by FACS according to their lipid composition were performed. Skin tissue sections isolated from healthy individuals or from patients diagnosed with cSCC were used to evaluate the sphingolipid composition in vivo after toxin staining and confocal microscopy. To assess the influence of sphingolipid composition on cell state, dHFs treated with the Cer synthase inhibitor FB1 or lentiviral stable cell lines overexpressing GSL-synthesizing enzymes were analyzed by scRNA-seq.

Full materials and methods are available as supplementary materials (*37*).

REFERENCES AND NOTES

1. D. Wang, S. Bodovitz, Single cell analysis: The new frontier in 'omics'. *Trends Biotechnol.* **28**, 281–290 (2010). doi: 10.1016/j.tibtech.2010.03.002; pmid: 20434785
2. O. Symmons, A. Raj, What's luck got to do with it: Single cells, multiple fates, and biological nondeterminism. *Mol. Cell* **62**, 788–802 (2016). doi: 10.1016/j.molcel.2016.05.023; pmid: 27259209
3. J. P. Junker, A. van Oudenaarden, Every cell is special: Genome-wide studies add a new dimension to single-cell biology. *Cell* **157**, 8–11 (2014). doi: 10.1016/j.cell.2014.02.010; pmid: 24679522
4. Q. Chen, J. Shi, Y. Tao, M. Zernicka-Goetz, Tracing the origin of heterogeneity and symmetry breaking in the early mammalian embryo. *Nat. Commun.* **9**, 1819 (2018). doi: 10.1038/s41467-018-04155-2; pmid: 29739935
5. M. Zinner, I. Lukonin, P. Liberali, Design principles of tissue organisation: How single cells coordinate across scales. *Curr. Opin. Cell Biol.* **67**, 37–45 (2020). doi: 10.1016/j.ceb.2020.07.004; pmid: 32889170

6. R. R. Driskell, F. M. Watt, Understanding fibroblast heterogeneity in the skin. *Trends Cell Biol.* **25**, 92–99 (2015). doi: 10.1016/j.tcb.2014.10.001; pmid: 25455110
7. J. M. Sorrell, A. I. Caplan, Fibroblast heterogeneity: More than skin deep. *J. Cell Sci.* **117**, 667–675 (2004). doi: 10.1242/jcs.01005; pmid: 14754903
8. F. M. Watt, H. Fujiwara, Cell-extracellular matrix interactions in normal and diseased skin. *Cold Spring Harb. Perspect. Biol.* **3**, a005124 (2011). doi: 10.1101/cshperspect.a005124; pmid: 21441589
9. C. Philippeos *et al*., Spatial and single-cell transcriptional profiling identifies functionally distinct human dermal fibroblast subpopulations. *J. Invest. Dermatol.* **138**, 811–825 (2018). doi: 10.1016/j.jid.2018.01.016; pmid: 29391249
10. E. Rognoni *et al*., Fibroblast state switching orchestrates dermal maturation and wound healing. *Mol. Syst. Biol.* **14**, e8174 (2018). doi: 10.15252/msb.20178174; pmid: 30158243
11. A. M. Ascensión, S. Fuertes-Álvarez, O. Ibañez-Solé, A. Izeta, M. J. Araúzo-Bravo, Human dermal fibroblast subpopulations are conserved across single-cell RNA sequencing studies. *J. Invest. Dermatol.* **141**, 1735–1744.e35 (2021). doi: 10.1016/j.jid.2020.11.028; pmid: 33385399
12. M. Adler *et al*., Principles of cell circuits for tissue repair and fibrosis. *iScience* **23**, 100841 (2020). doi: 10.1016/j.isci.2020.100841; pmid: 32058955
13. E. Rognoni, F. M. Watt, Skin cell heterogeneity in development, wound healing, and cancer. *Trends Cell Biol.* **28**, 709–722 (2018). doi: 10.1016/j.tcb.2018.05.002; pmid: 29807713
14. M. F. Griffin, H. E. desJardins-Park, S. Mascharak, M. R. Borrelli, M. T. Longaker, Understanding the impact of fibroblast heterogeneity on skin fibrosis. *Dis. Model. Mech.* **13**, dmm044164 (2020). doi: 10.1242/dmm.044164; pmid: 32541065
15. G. Biffi, D. A. Tuveson, Diversity and biology of cancer-associated fibroblasts. *Physiol. Rev.* **101**, 147–176 (2021). doi: 10.1152/physrev.00048.2019; pmid: 32466724
16. C. F. Guerrero-Juarez *et al*., Single-cell analysis reveals fibroblast heterogeneity and myeloid-derived adipocyte progenitors in murine skin wounds. *Nat. Commun.* **10**, 650 (2019). doi: 10.1038/s41467-018-08247-x; pmid: 30737373
17. Y. Rinkevich *et al*., Skin fibrosis. Identification and isolation of a dermal lineage with intrinsic fibrogenic potential. *Science* **348**, aaa2151 (2015). doi: 10.1126/science.aaa2151; pmid: 25883361
18. E. Rognoni *et al*., Inhibition of β-catenin signalling in dermal fibroblasts enhances hair follicle regeneration during wound healing. *Development* **143**, 2522–2535 (2016). doi: 10.1242/dev.131797; pmid: 27287810
19. T. S. Cliff, S. Dalton, Metabolic switching and cell fate decisions: Implications for pluripotency, reprogramming and development. *Curr. Opin. Genet. Dev.* **46**, 44–49 (2017). doi: 10.1016/j.gde.2017.06.008; pmid: 28662447
20. D. Russo, L. Capolupo, J. S. Loomba, L. Sticco, G. D'Angelo, Glycosphingolipid metabolism in cell fate specification. *J. Cell Sci.* **131**, jcs219204 (2018). doi: 10.1242/jcs.219204; pmid: 30559216
21. B. Snijder *et al*., Population context determines cell-to-cell variability in endocytosis and virus infection. *Nature* **461**, 520–523 (2009). doi: 10.1038/nature08282; pmid: 19710653
22. M. Frechin *et al*., Cell-intrinsic adaptation of lipid composition to local crowding drives social behaviour. *Nature* **523**, 88–91 (2015). doi: 10.1038/nature14429; pmid: 26009010
23. M. Denz *et al*., Cell cycle dependent changes in the plasma membrane organization of mammalian cells. *Biochim. Biophys. Acta Biomembr.* **1859**, 350–359 (2017). doi: 10.1016/j.bbamem.2016.12.004; pmid: 27993567
24. D. Russo *et al*., Glycosphingolipid metabolic reprogramming drives neural differentiation. *EMBO J.* **37**, e97674 (2018). doi: 10.15252/embj.201797674; pmid: 29282205
25. M. Vietri Rudan, A. Mishra, C. Klose, U. S. Eggert, F. M. Watt, Human epidermal stem cell differentiation is modulated by specific lipid subspecies. *Proc. Natl. Acad. Sci. U.S.A.* **117**, 22173–22182 (2020). doi: 10.1073/pnas.2011310117; pmid: 32843345
26. R. Zenobi, Single-cell metabolomics: Analytical and biological perspectives. *Science* **342**, 1243259 (2013). doi: 10.1126/science.1243259; pmid: 24311695
27. C. Thiele, K. Wunderling, P. Leyendecker, Multiplexed and single cell tracing of lipid metabolism. *Nat. Methods* **16**, 1123–1130 (2019). doi: 10.1038/s41592-019-0593-6; pmid: 31611692
28. L. Rappez *et al*., SpaceM reveals metabolic states of single cells. *Nat. Methods* **18**, 799–805 (2021). doi: 10.1038/s41592-021-01198-0; pmid: 34226721
29. J. L. Norris, R. M. Caprioli, Analysis of tissue specimens by matrix-assisted laser desorption/ionization imaging mass spectrometry in biological and clinical research. *Chem. Rev.* **113**, 2309–2342 (2013). doi: 10.1021/cr3004295; pmid: 23394164
30. Y. Schober, S. Guenther, B. Spengler, A. Römpp, Single cell matrix-assisted laser desorption/ionization mass spectrometry imaging. *Anal. Chem.* **84**, 6293–6297 (2012). doi: 10.1021/ac301337h; pmid: 22816738
31. M. E. Dueñas, J. J. Essner, Y. J. Lee, 3D MALDI mass spectrometry imaging of a single cell: Spatial mapping of lipids in the embryonic development of zebrafish. *Sci. Rep.* **7**, 14946 (2017). doi: 10.1038/s41598-017-14949-x; pmid: 29097697
32. A. Zavalin *et al*., Direct imaging of single cells and tissue at sub-cellular spatial resolution using transmission geometry MALDI MS. *J. Mass Spectrom.* **47**, 1473–1481 (2012). doi: 10.1002/jms.3108; pmid: 23147824
33. M. Kompauer, S. Heiles, B. Spengler, Atmospheric pressure MALDI mass spectrometry imaging of tissues and cells at 1.4-μm lateral resolution. *Nat. Methods* **14**, 90–96 (2017). doi: 10.1038/nmeth.4071; pmid: 27842060
34. M. Niehaus, J. Soltwisch, M. E. Belov, K. Dreisewerd, Transmission-mode MALDI-2 mass spectrometry imaging of cells and tissues at subcellular resolution. *Nat. Methods* **16**, 925–931 (2019). doi: 10.1038/s41592-019-0536-2; pmid: 31451764
35. E. Sugiyama, I. Yao, M. Setou, Visualization of local phosphatidylcholine synthesis within hippocampal neurons using a compartmentalized culture system and imaging mass spectrometry. *Biochem. Biophys. Res. Commun.* **495**, 1048–1054 (2018). doi: 10.1016/j.bbrc.2017.11.108; pmid: 29162450
36. D. R. Bhandari, G. Coliva, M. Fedorova, B. Spengler, "Single cell analysis by high-resolution atmospheric-pressure MALDI MS imaging," in: *Single Cell Metabolism: Methods and Protocols*, B. Shrestha, Ed. (Springer, 2020); pp. 103–111.
37. Materials and methods are available as supplementary materials.
38. J. C. M. Holthuis, A. K. Menon, Lipid landscapes and pipelines in membrane homeostasis. *Nature* **510**, 48–57 (2014). doi: 10.1038/nature13474; pmid: 24899304
39. L. Pelkmans, Cell Biology. Using cell-to-cell variability—A new era in molecular biology. *Science* **336**, 425–426 (2012). doi: 10.1126/science.1222161; pmid: 22539709
40. M. Jacewicz, H. Clausen, E. Nudelman, A. Donohue-Rolfe, G. T. Keusch, Pathogenesis of shigella diarrhea. XI. Isolation of a shigella toxin-binding glycolipid from rabbit jejunum and HeLa cells and its identification as globotriaosylceramide. *J. Exp. Med.* **163**, 1391–1404 (1986). doi: 10.1084/jem.163.6.1391; pmid: 3519828
41. J. Müthing, C. H. Schweppe, H. Karch, A. W. Friedrich, Shiga toxins, glycosphingolipid diversity, and endothelial cell injury. *Thromb. Haemost.* **101**, 252–264 (2009). doi: 10.1160/TH08-05-0317; pmid: 19190807
42. S. van Heyningen; Heyningen S Van, Cholera toxin: Interaction of subunits with ganglioside GM1. *Science* **183**, 656–657 (1974). doi: 10.1126/science.183.4125.656; pmid: 4810267
43. E. Wang, W. P. Norred, C. W. Bacon, R. T. Riley, A. H. Merrill Jr., Inhibition of sphingolipid biosynthesis by fumonisins. Implications for diseases associated with Fusarium moniliforme. *J. Biol. Chem.* **266**, 14486–14490 (1991). doi: 10.1016/S0021-9258(18)98712-0; pmid: 1860857
44. J. Inokuchi, K. Momosaki, H. Shimeno, A. Nagamatsu, N. S. Radin, Effects of D-threo-PDMP, an inhibitor of glucosylceramide synthetase, on expression of cell surface glycolipid antigen and binding to adhesive proteins by B16 melanoma cells. *J. Cell. Physiol.* **141**, 573–583 (1989). doi: 10.1002/jcp.1041410316; pmid: 2531751
45. P. Liberali, B. Snijder, L. Pelkmans, A hierarchical map of regulatory genetic interactions in membrane trafficking. *Cell* **157**, 1473–1487 (2014). doi: 10.1016/j.cell.2014.04.029; pmid: 24906158
46. Y. A. Hannun, L. M. Obeid, Sphingolipids and their metabolism in physiology and disease. *Nat. Rev. Mol. Cell Biol.* **19**, 175–191 (2018). doi: 10.1038/nrm.2017.107; pmid: 29165427
47. L. Haghverdi, F. Buettner, F. J. Theis, Diffusion maps for high-dimensional single-cell analysis of differentiation data. *Bioinformatics* **31**, 2989–2998 (2015). doi: 10.1093/bioinformatics/btv325; pmid: 26002886
48. F. A. Wolf *et al*., PAGA: Graph abstraction reconciles clustering with trajectory inference through a topology preserving map of single cells. *Genome Biol.* **20**, 59 (2019). doi: 10.1186/s13059-019-1663-x; pmid: 30890159
49. R. R. Driskell *et al*., Distinct fibroblast lineages determine dermal architecture in skin development and repair. *Nature* **504**, 277–281 (2013). doi: 10.1038/nature12783; pmid: 24336287
50. R. A. Harper, G. Grove, Human skin fibroblasts derived from papillary and reticular dermis: Differences in growth potential in vitro. *Science* **204**, 526–527 (1979). doi: 10.1126/science.432659; pmid: 432659
51. D. G. Janson, G. Saintigny, A. van Adrichem, C. Mahé, A. El Ghalbzouri, Different gene expression patterns in human papillary and reticular fibroblasts. *J. Invest. Dermatol.* **132**, 2565–2572 (2012). doi: 10.1038/jid.2012.192; pmid: 22696053
52. H. Y. Chang *et al*., Gene expression signature of fibroblast serum response predicts human cancer progression: Similarities between tumors and wounds. *PLOS Biol.* **2**, E7 (2004). doi: 10.1371/journal.pbio.0020007; pmid: 14737219
53. P. Bordignon *et al*., Dualism of FGF and TGF-β signaling in heterogeneous cancer-associated fibroblast activation with ETV1 as a critical determinant. *Cell Rep.* **28**, 2358–2372.e6 (2019). doi: 10.1016/j.celrep.2019.07.092; pmid: 31461652
54. L. Gerosa *et al*., Receptor-driven ERK pulses reconfigure MAPK signaling and enable persistence of drug-adapted BRAF-mutant melanoma cells. *Cell Syst.* **11**, 478–494.e9 (2020). doi: 10.1016/j.cels.2020.10.002; pmid: 33113355
55. S. Abbasi *et al*., Distinct regulatory programs control the latent regenerative potential of dermal fibroblasts during wound healing. *Cell Stem Cell* **27**, 396–412.e6 (2020). doi: 10.1016/j.stem.2020.07.008; pmid: 32755548
56. M. V. Plikus *et al*., Regeneration of fat cells from myofibroblasts during wound healing. *Science* **355**, 748–752 (2017). doi: 10.1126/science.aai8792; pmid: 28059714
57. D. Jiang, Y. Rinkevich, Scars or regeneration? Dermal fibroblasts as drivers of diverse skin wound responses. *Int. J. Mol. Sci.* **21**, 617 (2020). doi: 10.3390/ijms21020617; pmid: 31963533
58. B. A. Kramer, L. Pelkmans, Cellular state determines the multimodal signaling response of single cells. *bioRxiv*. 2019. p. 2019.12.18.880930. doi: 10.1101/2019.12.18.880930
59. A. R. Lederer, G. La Manno, The emergence and promise of single-cell temporal-omics approaches. *Curr. Opin. Biotechnol.* **63**, 70–78 (2020). doi: 10.1016/j.copbio.2019.12.005; pmid: 31918114
60. W. Chen *et al*., Genome-wide molecular recording using Live-seq. *bioRxiv*. 2021. p. 2021.03.24.436752. doi: 10.1101/2021.03.24.436752
61. M. Schuhmacher *et al*., Live-cell lipid biochemistry reveals a role of diacylglycerol side-chain composition for cellular lipid dynamics and protein affinities. *Proc. Natl. Acad. Sci. U.S.A.* **117**, 7729–7738 (2020). doi: 10.1073/pnas.1912684117; pmid: 32213584
62. L. Capolupo, "Untargeted lipidomics of primary human skin fibroblasts" (NIH Metabolomics Workbench, 2020); https://www.metabolomicsworkbench.org/data/DRCCMetadata.php?Mode=Project&ProjectID=PR001087.
63. L. Capolupo, O. Burri, R. Guiet, Cellpose model for digital phase contrast images for: Sphingolipids control dermal fibroblast heterogeneity. Zenodo (2022); https://zenodo.org/record/6023317#.YjTffurMKUk.
64. L. Capolupo, Digital phase contrast on primary dermal human fibroblasts cells for: Sphingolipids control dermal fibroblast heterogeneity, Zenodo (2022); https://zenodo.org/record/5996883#.YjTfourMKUk.
65. L. Capolupo, I. Khven, A. R. Lederer, G. La Manno, G. D'Angelo, Notebooks for analysis of single-cell RNA sequencing datasets and CELLMA lipotype state transition inference modeling for: Sphingolipids control dermal fibroblast heterogeneity, Zenodo (2022); https://zenodo.org/record/6245944#.YjTf7erMKUk.

ACKNOWLEDGMENTS

We thank B. Deplancke, P. Seetharaman, D. Russo, C. Dibner, Y. Hannun, C. Luberto, and S. Linnarsson for critically reading the manuscript; H. H. Schede for the help with MALDI-MSI image analysis; and L. Talamanca for the comments on mathematical notation. **Funding:** G.L.M. and I.K. were supported by the Swiss National Science Foundation (grants CRSK-3_190495 and PZ00P3_193445). G.L.M. was supported by the School of Life Sciences, EPFL. G.D. acknowledges financial support from the Swiss Cancer League (grant KFS-4999-02-2020), the EPFL institutional fund, the Kristian Gerhard Jebsen Foundation, and the Swiss National Science Foundation (SNSF grant 310030_184926). L.M. and G.P.D. were supported by the Swiss National Science Foundation (grant 310030B_176404), the National Institutes of Health (NIH grant R01AR039190; the content does not necessarily represent the official views of the NIH), and the European Union's Horizon 2020 research and innovation program (Marie Skłodowska-Curie grant 859860). **Author contributions:**

L.C. developed the idea, conducted the experiments, and wrote the manuscript. I.K. participated in the development of the idea, conducted image and scRNA-seq analyses, and performed the scRNA-seq experiments. A.R.L. conceptualized and contributed to implementing the CELLMA model. L.M. supported L.C. in experiments on DN fibroblast lines. G.G. generated the GM3S and Gb4S OE fibroblast lines. S.H. provided technical assistance. F.R. performed initial lipid data analysis. J.P.M. performed targeted and untargeted lipidomics. A.P.B. and S.R.E. assisted with MALDI-MSI. R.G. performed FISH analysis. O.B. helped with live imaging experiments. J.M. and J.D. provided ShTxB2e toxin. K.H. contributed to discussions and provided reagents. F.K. and M.G. provided skin tissue sections. D.R.B. and B.S. performed AP-SMALDI10 and AP-SMALDI5 AF experiments. R.M.A.H. provided assistance with MALDI-MSI data treatment. G.P.D. contributed to discussions and provided reagents for dHF heterogeneity. G.L.M. and G.D.A. developed the idea, designed and supervised the entire project, analyzed the data, and wrote the manuscript. **Competing interests:** B.S is a consultant and D.R.B. is a part-time employee of TransMIT GmbH, Giessen, Germany. The authors declare no competing financial interests. **Data availability:** All data are available in the main text and supplementary materials and at (*62*–*65*). Further information and requests for resources and reagents can be directed to the corresponding authors. Any requests for toxins and antibodies can be directed to the corresponding authors or to the contact listed in table S4. Sequencing data are available on the Gene Expression Omnibus database under accession no. GSE167209. Lipid images are available at https://metaspace2020.eu/project/capolupo-2022.

SUPPLEMENTARY MATERIALS

science.org/doi/10.1126/science.abh1623
Materials and Methods
Supplementary Note 1
Figs. S1 to S10
Tables S1 to S6
References (*66*–*78*)
Movie S1
MDAR Reproducibility Checklist

View/request a protocol for this paper from *Bio-protocol*.

20 February 2021; resubmitted 11 November 2021
Accepted 7 March 2022
10.1126/science.abh1623